EES Batteries

PAPER

View Article Online
View Journal

Check for updates

Cite this: DOI: 10.1039/d6eb00020g

Calendar and cycle ageing of commercial sodium-ion cells with layered oxide cathodes: how does operation influence degradation modes?

Julius Bahrke, *[a] Mathias Rehm, [a] Johannes Natterer, [a,b] Caroline Wendlandt [a] and Andreas Jossen [a]

Received 22nd January 2026,
Accepted 20th April 2026

DOI: 10.1039/d6eb00020g

rsc.li/EESBatteries

Despite the continuous success of lithium-ion batteries, sodium-ion batteries pose a relevant alternative to lithium-based storage systems. Abundant resources that can be obtained by more environmentally friendly processes make sodium-ion batteries a feasible alternative to lithium-ion batteries for large-scale applications. However, the ageing behaviour of sodium-ion batteries and their subsequent degradation modes have not yet been fully investigated. In this work, commercial sodium-ion batteries are aged under various conditions to study the impact of state-of-charge, depth of discharge, temperature, and current rate on ageing. For this study, we investigated the initial electrical and electrochemical parameters of 94 commercial cells with layered oxide cathodes and hard carbon anodes. From these cells, we selected and aged 70 cells for almost two years or up to 5000 equivalent full cycles. We demonstrate that sodium-plating on the anode surface poses a relevant failure mechanism in sodium-ion batteries throughout all operating conditions. We used degradation-mode analysis to identify the main drivers for degradation. Capacity fade is arguably driven by loss of active material at the cathode, which is more dominant when operating or storing in high state-of-charge ranges. In contrast to lithium-ion batteries, the loss of charge carrier inventory is not the main driver for capacity fade in sodium-ion batteries. Loss of active material from the anode occurs but it plays a minor role. However, anode material loss is more pronounced when operating or storing in low state-of-charge ranges.

Broader context

Reliable energy storage is essential for the transition to carbon neutral energy supply. Lithium-ion supply chains rely on scarce or environmentally intensive raw materials. Sodium-ion batteries offer a lower-cost alternative that can reduce resource risk, but systematic evidence on how they age under realistic operating conditions remains limited. We ask: how do sodium-ion cells age within different operating windows, and what causes the loss of capacity and power? We subjected commercial 18650-format cells to several thousand cycles while varying depth of discharge, C-rate, and state of charge, and stored cells at different states of charge and temperatures. We first show that cell-to-cell variability remains a challenge in commercially available cells. Some cells exhibit metallic sodium deposition on the negative electrode, which can increase safety risk and leads to unpredictable ageing. This behaviour appears to be driven more by initial cell variation than by the operating conditions tested. When sodium deposition is minimal, ageing is dominated by degradation of the positive electrode, which is more pronounced at high states of charge. Loss of active material at the negative electrode is smaller overall but increases at lower states of charge. These findings help define safer operating windows for sodium-ion batteries and point to priorities for future materials and cell-design research.

1 Introduction

The continuous growth of demand for energy storage solutions leads to the further popularity of lithium-ion batteries (LIBs), which inevitably increases the necessity of stable supply chains and reduction of ecological impact of raw materials. The extraction of nickel and lithium has a substantial ecological impact, while the availability of cobalt and lithium remains critical, with supply chain volatility continuing to increase. This leads to a high economic risk for manufacturers and accelerates price uncertainty.[1] Thus, research on alternative storage technologies continues, despite extensive knowledge on and commercialization of LIBs.

Sodium-ion batteries (SIBs) provide a promising alternative to LIBs due to the abundance of resources, similar production processes, as well as similar operating principles as LIBs.[2,3]

---

[a] *Technical University of Munich (TUM), TUM School of Engineering and Design, Department of Energy and Process Engineering, Chair of Electrical Energy Storage Technology (EES), Arcisstr. 21, 80333 Munich, Germany. E-mail: julius.bahrke@tum.de*

[b] *Infineon Technologies AG, Am Campeon 1-15, 85579 Neubiberg, Germany*

Due to these similarities, SIBs are often discussed as a drop-in technology.[4] However, key differences persist.

The larger ionic radius of sodium ions compared to lithium ions leads to different storage mechanisms. Hard carbon (HC) is the most commonly used anode material for SIBs due to its ability to accommodate the larger sodium ions in comparison to graphite. HC exhibits a different intercalation mechanism compared to graphite, leading to a sloping voltage region in low states of sodiation before moving into a plateau region at higher sodiation levels.[5,6] These aspects make the ageing behaviour of SIBs an open and not fully understood area of research.

Beyond HC, further anode materials such as MoS_2-based composites are being investigated for SIBs.[7] However, these anode materials still suffer from mechanical instability, which can be improved by further anode engineering.[8]

Furthermore, layered metal oxides (LMOs) present a promising cathode material for SIBs due to high voltage, high capacity, and readily scalable manufacturing.[9] Current research on LMO-based cathodes for SIBs focuses on interface stabilization and structural modification strategies to enhance long-term cycling performance.[10]

However, SIBs need to compare to LIBs in multiple fields. One key aspect is the potential lifetime during application and understanding of fundamental ageing processes.

Numerous studies have investigated the ageing behaviour of LIBs under various cycling protocols as well as calendar ageing. These studies include the influence of temperature, C-rate, depth of discharge (DOD), mean state-of-charge (SOC) for cycling and SOC, as well as temperature for calendar ageing.[11–15]

Birkl *et al.*[16] defined the ageing mechanisms and corresponding degradation modes for LIBs, which lead to power and capacity fade. The degradation modes include loss of active material at the anode and the cathode and loss of lithium inventory. In this work they are referred to as loss of active material at the negative electrode (LAM_{an}), loss of active material at the positive electrode (LAM_{cat}), and loss of charge carrier inventory (LI), respectively. To ensure better transferability, we use the term of "loss of charge carrier inventory" as it applies to both SIBs and LIBs.

The literature provides three general approaches to determine degradation modes in batteries *via* changes in the open circuit voltage (OCV) curve. The first approach is tracking the characteristic peaks in the differential voltage (DV) or incremental capacity (IC) curve throughout ageing.[17,18] The second approach is using synthetic OCV-modelling where the influence of ageing modes on the open circuit potentials (OCPs) of the individual electrodes is simulated to recreate the OCV.[19] The third approach uses OCP measurements of the individual pristine electrodes, which are then shifted and scaled to recreate the full-cell OCV measured at various ageing stages. The shifting and scaling parameters define the ageing modes.[16] In this work, we adopt this electrode-OCP-based shifting-and-scaling approach, as this has been proven to determine degradation modes and was implemented in a framework in our previous work. In this work, we demonstrated that the application of degradation-mode analysis (DMA) on SIBs is possible using OCP measurements of the individual pristine electrodes to recreate the full-cell voltage. Furthermore, we showed that the shifting and scaling of the OCPs can be used to recreate the aged full-cell OCV and verified this with measurements of aged OCPs.[20]

While LIB ageing under cycling and storage conditions is well established, SIB ageing studies are comparatively sparse and primarily focus on capacity fade and resistance growth. In particular, for HC-LMO full cells, there is a lack of systematic investigations that quantify the contributions of inventory loss and anode-/cathode-related loss of active material (LAM) across relevant cycling and calendar ageing conditions. To the best of our knowledge, this significantly limits the necessary mechanistic interpretation approaches and potential transferability on lifetime optimisation during operation.

Laufen *et al.*[21] presented a multi-method characterisation of the same cell used in this study. They included ageing data for cycle ageing at various C-rates and showed that their investigated SIBs have robust cycling performance. However, the authors reported that several cells stopped operating because the current interruption device (CID) was triggered due to gassing. Klick *et al.*[22] conducted a comprehensive study on the influence of cycling conditions on SIB ageing and identified the influence of DOD, C-rate, and temperature on the overall capacity fade and resistance increase. Furthermore, they generated a dataset of synthetic OCVs by applying multiple combinations of degradation modes and their influence on the OCPs. The degradation modes were then determined by comparing to the ICA curves of the aged cells. Dubarry and Beck[23] presented the transferability of DMA on SIBs with a HC anode and an NVPF cathode, by synthesizing degradation-mode influence on OCPs.

Even though the outlined studies contribute to a fundamental understanding of mechanistic ageing quantification in SiBs, they fall short of providing degradation-mode-resolved quantification across both cycle and calendar ageing. To the best of our knowledge, a systematic evaluation and analysis of HC-LMO degradation-mode mappings has not yet been presented in the literature.

Building upon these advancements and the shortcomings of the current literature regarding DM mapping in SIBs, we present in this work a detailed investigation of the influence of cycle and calendar ageing conditions on the ageing behaviour and to establish a degradation-mode map for HC-LMO SIB full cells. We apply DMA using OCP measurements of the individual early-life electrodes to determine the degradation modes and their progression during ageing. The influence of DOD, C-rate, and average SOC as cycling conditions on the ageing behaviour is investigated while for calendar ageing the influence of storage SOC and temperature is studied. To the best of our knowledge, this is the first systematic degradation-mode mapping for HC-LMO SIB full cells, covering both cycle (DOD, C-rate, mean SOC) and calendar (storage SOC, temperature) ageing based on electrode-OCP-derived DMA.

2 Experimental and methodology

2.1 Investigated cells

In this work, we investigate a SIB cell that was among the first to be made commercially available. The cell is an 18650-format cell manufactured by Shenzhen Mushang Electronics Co., Ltd with a nominal capacity of 1.25 A h and a voltage range of 1.5 V to 3.8 V. Previous work has investigated this cell type in depth regarding its chemistry, and electrical, thermal and electrochemical behaviour at both the cell level and material level.[21,24–29] The specifications of the cell are given in Table 1. For this study, we characterised 94 cells initially before investigating 70 cells regarding their cycle and calendar ageing behaviour. The cells showed great variance in electric behaviour and were grouped so that the variance in each test point (TP) was similar, regarding capacity, resistance and thermal properties, as described in sections 3.1 and 3.2.

2.2 Cell preparation and test setup

For cycle ageing, all cells were connected in a four-wire contact configuration. Contacts were welded to each cell tab to ensure uniform and low contact resistance. One welded terminal was assigned to the sensing circuit and an additional welded terminal to the power circuit, providing separate paths for measurement and load. This minimises the influence of contact resistance on voltage measurements during current loads. Cell temperature was measured at the negative cell tab using a thermistor sensor, which was insulated from environmental influences with a 10 mm-thick ArmaFlex material layer. The terminals of cells for calendar ageing were not welded as no current load was applied during storage. Instead, these cells were placed in contact with custom cell holders during check-up (CU), using golden contact pins with a four-wire contact configuration (Feinmetall GmbH). The temperature of the calendar cells was measured during the CU using a thermistor sensor placed at the centre of the cell-wall surface using heat-resistant Kapton tape. All tests were performed using a BINDER KT-170 climate chamber and a BaSyTec CTS 32 Channel 5 A battery tester.

2.3 Initial measurements

We defined an initial-measurements protocol to determine the state of the cells. The protocol included the following steps, with each constant-current constant-voltage (CCCV) phase performed at 0.5C during the constant-current (CC) stage and a 0.05C cutoff current during the constant-voltage (CV) stage between 1.5 V and 3.8 V:

- Initial CCCV discharge to 1.5 V.
- 10 full cycles of CCCV charge and discharge.
- Hybrid Pulse Power Characterisation (HPPC) at 90%, 50% and 10% with 0.1C and 1C to determine R_{DC}.
- Full CCCV charge and consecutive CC discharge to 50%.
- Rest for at least 12 h at 25 °C.
- Galvanostatic electrochemical impedance spectroscopy (GEIS) measurement at 50% SOC based on the capacity determined during the last discharge step from 100 kHz to 10 mHz with 50 mA amplitude.

The capacity was determined during the final discharge of the 10 initial cycles. The procedure was performed in a climate chamber at 25 °C. 10 cycles were chosen to ensure that the cells are as homogeneous as possible, both electrochemically and thermally, before starting the ageing study. The GEIS measurement was used to determine two characteristic points in the impedance spectrum. The first point is the real part of the impedance where the imaginary part is equal to zero, which will be called real impedance at zero crossing (R_{ZC}). This point is often referred to as the ohmic resistance of the cell.[30–33]

The second point is the real part of the impedance at the beginning of the diffusive tail, where the imaginary part of the impedance forms a local minimum, *i.e.* the R_{ZC} value subtracted from the real impedance at the diffusive-tail minimum. In this work, it is referred to as real impedance at the beginning of the diffusive tail (R_{POL}) and describes the diameter of the quasi-semi-circle of the impedance. In LIBs, this value is often associated, among other factors, with charge transfer and the solid electrolyte interface (SEI).[33–36]

Table 1 Specifications of the investigated cell as given by the manufacturer's datasheet

Manufacturer	Shenzhen Mushang Electronics Co., Ltd
Cell type	18650
C_{nom}	1.25 A h
U_{nom}	3.0 V
U_{min}	1.5 V
U_{max}	3.8 V
$I_{\mathrm{max,\ charge}}$	5 C
$I_{\mathrm{max,\ discharge}}$	8 C
Chemistry(cathode|anode)	LMO[a]|hard carbon

[a] Layered metal oxide is Na $\mathrm{Mn}_x\mathrm{Fe}_y\mathrm{Ni}_z\mathrm{O}_2$ with an Mn/Fe/Ni ratio of 1 : 1 : 1.[21]

2.4 Ageing study

The ageing study is structured as follows. Before starting the ageing procedure, the initial check-up (CU_0) was performed in addition to the initial characterisation and will be referred to as the beginning of test (BOT). Afterwards, we performed the ageing analysis. After each ageing section, a CU was conducted to assess the capacity state of health ($\mathrm{SOH}_{\mathrm{C}}$) and resistance state of health ($\mathrm{SOH}_{\mathrm{R}}$) for all cells until the ageing evaluation was concluded with a final CU at the end of test (EOT). $\mathrm{SOH}_{\mathrm{C}}$ and $\mathrm{SOH}_{\mathrm{R}}$ are defined as:

$$\mathrm{SOH}_{\mathrm{C}} = \frac{C_{\mathrm{act}}}{C_{\mathrm{init}}} \times 100\% \tag{1}$$

$$\mathrm{SOH}_{\mathrm{R}} = \frac{R_{\mathrm{act}}}{R_{\mathrm{init}}} \times 100\% \tag{2}$$

where C_{act} is the actual capacity determined during CU, C_{init} is the initial capacity determined during CU_0, R_{act} is the direct current resistance (R_{DC}) determined during CU after 10 s and R_{init} is the initial R_{DC} determined during CU_0.

Ageing sections can be divided into cycle and calendar ageing. The cycle ageing was carried out by performing a defined number of cycles within a specified SOC window and at a defined C-rate and temperature of 25 °C, whereas the calendar ageing was carried out by storing the cells at a specified SOC and temperature. For each ageing phase, at least three cells were aged under the same conditions to ensure reproducibility of results and to determine potential outliers.

2.4.1 Check-up procedure. During each ageing procedure, regular CUs were performed. The CU procedure was the same for calendar and cycle ageing, including the five steps listed below after allowing cells to rest for 2 h at 25 °C and conducting an initial CCCV discharge to 1.5 V at 0.5C.

I. First capacity check cycle (CapCC): CCCV charge at 0.5C to 3.8 V and CCCV discharge at 0.5C to 1.5 V with cutoff current of 0.05C during the CV phase.

II. Second CapCC, analogous to step I.

III. Galvanostatic intermittent titration technique (GITT) measurement: after CCCV charging, stepwise discharge in 5% steps at 1C until an end-of-discharge voltage of 1.5 V is reached in order to determine R_{DC}, with 5 min rest after each discharge step. Perform the same procedure in the charge direction until 3.8 V is reached.

IV. After CCCV discharge to 1.5 V and a 10 min pause, a pseudo-open circuit voltage (pOCV) measurement is carried out in the charge direction at 0.05C until 3.8 V is reached.

V. After a 10 min pause, a pOCV measurement in the discharge direction at 0.05C until 1.5 V is reached.

The CU procedure is shown in Fig. 1 with the corresponding relevant steps indicated as described previously. For capacity determination, the second cycle of the capacity check (step II) is used. The GITT measurement is performed to determine the internal resistance of the cells at different SOC levels.

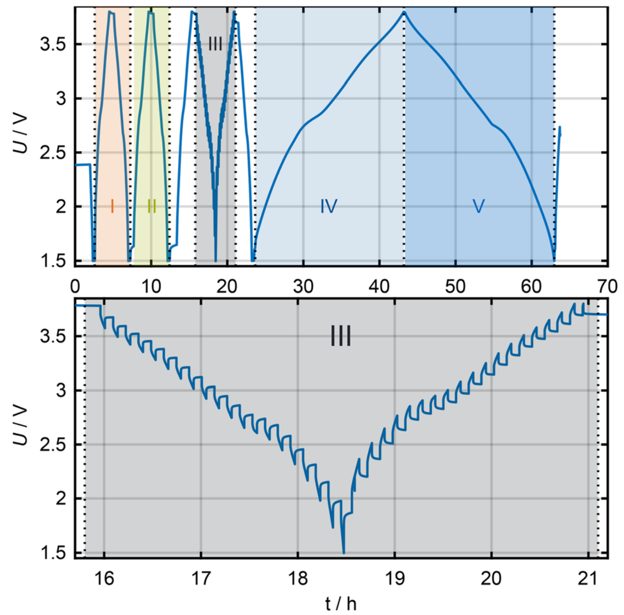

Fig. 1 Check-up procedure including relevant steps for capacity and efficiency determination (I & II), galvanostatic intermittent titration technique measurement (III), and pseudo-open circuit voltage measurement (IV & V).

The pOCV measurements are used to determine the voltage response at low current rates to analyse changes in electrode potentials and to perform DMA as described in section 2.5. Additionally, we investigated the coulombic efficiency (CE) during the two CapCCs. For this we divided the CCCV discharge capacity by the CCCV charge capacity from the same cycle as described in eqn (3). These CE values will be referred to as CE_{I} and $\mathrm{CE}_{\mathrm{II}}$ for the first and second CapCC, respectively. The temperature increase during the charging process of the CapCC was calculated as well and will be referred to as ΔT_{ChaI} and $\Delta T_{\mathrm{ChaII}}$ for the first and second CapCC, respectively.

$$\mathrm{CE} = \frac{Q_{\text{CCCV-discharge}}}{Q_{\text{CCCV-charge}}} \tag{3}$$

2.4.2 Cycle ageing protocol. The cycle ageing study was performed at 25 °C in a climate chamber. The cells were cycled under different test profiles (TPs), using varying SOC windows and current rates, to investigate the influence of these parameters on ageing. To compare their influence on ageing, we grouped them into three categories.

- The average SOC was investigated by cycling the cells at 1C and 20% DOD around various SOC levels.
- The DOD was investigated by cycling the cells at 1C around 50% SOC and DODs of 100%, 60% and 20%.
- The influence of the current was investigated by cycling the cells with C-rates of 0.5C, 1C and 2C between 0% and 100% SOC.

The different TPs are summarized in Table 2. The cycling was performed using CCCV charge and CCCV discharge to the voltage limits given in Table 2. The CV phase concluded when the current dropped below 0.05C. After each CV phase, a rest period was applied. The rest period was dependent on the duration of the CV phase. The total duration of the CV phase and the subsequent rest period were kept constant in relation to the duration of the CC phase to ensure a similar influence during calendar ageing, and will be referred to as the time of constant voltage phase plus subsequent pause ($t_{\mathrm{CV+p}}$). At a C-rate of 1C, this total duration was 1200 s and was scaled linearly accordingly for the other C-rates and DODs. The duration times are given in Table 2. The number of cycles was adjusted according to the respective DOD, such that a theoretical equivalent of 200 full cycles was

Table 2 Overview of the different cycle ageing test points with corresponding SOC windows, C-rates, voltage limits and the duration of the CV phase combined with the subsequent pause phase. Four cells were cycled in TPs 1, 2, 3, 4, 5 and 9. Three cells were cycled in TPs 6, 7 and 8

TP	Start SoC	End SoC	C-rate	Lower voltage	Upper voltage	$t_{\mathrm{CV+p}}$
1	0%	100%	1C	1.5 V	3.8 V	1200 s
2	0%	100%	2C	1.5 V	3.8 V	600 s
3	0%	100%	0.5C	1.5 V	3.8 V	2400 s
4	20%	80%	1C	2.358 V	3.475 V	720 s
5	0%	20%	1C	1.5 V	2.455 V	240 s
6	20%	40%	1C	2.358 V	2.822 V	240 s
7	40%	60%	1C	2.752 V	3.136 V	240 s
8	60%	80%	1C	3.105 V	3.475 V	240 s
9	80%	100%	1C	3.448 V	3.8 V	240 s

reached before conducting the CU. Accordingly, 200 cycles were performed for 100% DOD, 333 cycles for 60% DOD, and 1000 cycles for 20% DOD. For analysis of ageing trajectories, we refer to equivalent full cycles (EFCs), which are always considered in reference to the nominal capacity of the cell.

2.4.3 Calendar ageing.

The calendar ageing study was performed at 25 °C and 45 °C in climate chambers. The cells were stored at SOC levels in 20% increments between 10% and 90% at 25 °C, and at 10%, 50% and 90% at 45 °C. CUs were performed approximately every 60 days of storage. Three cells were stored at each TP.

2.5 Degradation-mode analysis

We performed a DMA to differentiate the degradation modes over the ageing period using the pOCV in the charge direction. The following is a short summary of the implementation process. For a thorough discussion of the algorithm, the settings and test-setup specifics used within this paper, please refer to our previous publication.[20] The half-cell OCPs used for the fitting procedure are obtained from a three-electrode setup with harvested active material from the BOT cell. Direct measurements using a coin-cell setup did not yield acceptable results due to side reactions leading to low coulombic efficiency. Since a three-electrode setup does not allow full (de-)sodiation of the electrode material without violating the voltage boundaries of the full cell, only partial OCPs could be obtained. Therefore, to ensure the OCPs are sufficient to reconstruct the pOCV at the BOT, the fitting is performed in a limited SOC range of 5% to 95% SOC.[37] To fit the OCV, we used the genetic algorithm. The maximum number of attempts was set to 20 and the maximum number of attempts to be accepted was set to 15. An attempt was accepted if the root mean square error (RMSE) between measured and reconstructed pOCV values was below 8 mV. These OCPs are scaled and shifted such that the difference between the measured pOCV and the reconstructed OCV is minimised.[16,37] Then, the degradation modes $\mathrm{LAM_{an}}$ and $\mathrm{LAM_{cat}}$ can be determined by comparing the scaling factor α of the respective electrodes over the ageing period to the scaling factor at the BOT. We note that in our case the scaling factors are referenced with respect to the SOC of the cell in its current ageing state. Thus, the loss of active material at a specific electrode ($\mathrm{LAM_{el}}$) is given as:

$$\begin{aligned}\mathrm{LAM_{el}} &= \frac{C_{\mathrm{el,ini}} - C_{\mathrm{el}}}{C_{\mathrm{el,ini}}} \\ &= \frac{\alpha_{\mathrm{el,ini}} \cdot C_{\mathrm{full,ini}} - \alpha_{\mathrm{el}} \cdot C_{\mathrm{full}}}{\alpha_{\mathrm{el,ini}} \cdot C_{\mathrm{full,ini}}} \quad \text{with el} \in \{\text{an, cat}\}\end{aligned} \tag{4}$$

The charge carrier inventory can be obtained by linking scaling factors α with shifting factors β in

$$C_{\mathrm{inv}} = (\alpha_{\mathrm{cat}} - \beta_{\mathrm{an}} + \beta_{\mathrm{cat}}) \cdot C_{\mathrm{full}}. \tag{5}$$

The LI is then computed as:

$$\mathrm{LI} = \frac{C_{\mathrm{inv,ini}} - C_{\mathrm{inv}}}{C_{\mathrm{inv,ini}}} \tag{6}$$

The cost function of the optimizer included a weighted sum of the difference between the measured and reconstructed pOCV and the difference between the measured and reconstructed DV. The cost function is given as:

$$\mathrm{Cost} = \sum_{n \in W_{\mathrm{OCV}}} \left(U^{\mathrm{est}}_{\mathrm{OCV},n} - U_{\mathrm{OCV},n}\right)^2 + \lambda \sum_{m \in W_{\mathrm{DV}}} \left(\mathrm{DV}^{\mathrm{est}}_{m} - \mathrm{DV}_{m}\right)^2, \tag{7}$$

where the indices are locked into the windows for the DV and the pOCV, respectively.[20] The factor λ is the weighting factor for the DV *versus* the pOCV and, in our case, is set to 50. The differential voltage analysis (DVA) is only fitted in an SOC window between 5% and 30%, while the OCV is fitted between 5% and 95%.

The principle of the DMA procedure is illustrated in Fig. 2 for a BOT cell.

The DMA algorithm employed in this work, which has been peer-reviewed and validated in our previous work, was applied to the aged cells from which T-cells were harvested. T-cells are three-electrode reference cells assembled from harvested electrode sheets of the aged full cells, enabling independent measurement of the anode and cathode half-cell OCPs. The fitting results of the algorithm could thus be confirmed. The modelled half-cell OCPs matched the measured OCPs from the T-cells.[20]

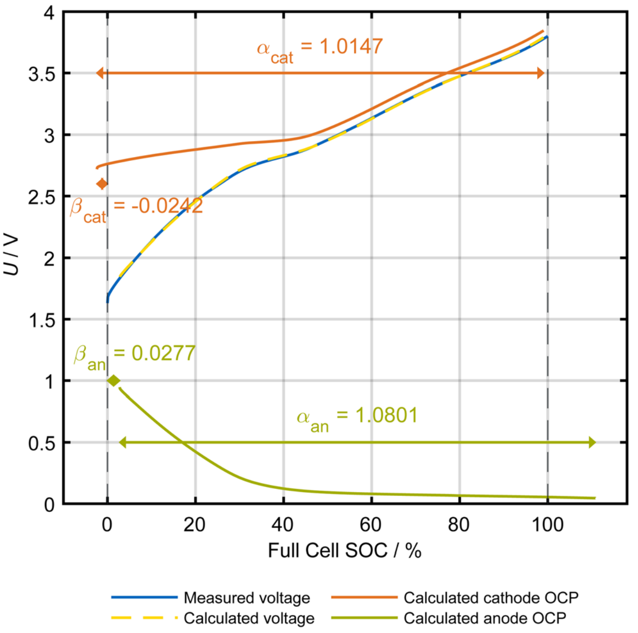

Fig. 2 Graphical representation of the degradation mode analysis. The measured pseudo-open circuit voltage (blue) is reconstructed (yellow) by shifting and scaling the electrode open circuit potential (green and orange) obtained from a T-cell measurement. The difference between measured and reconstructed pseudo-open circuit voltage as well as the differential voltage analysis is minimised to obtain the degradation modes. The shifting (β) and scaling (α) factors are illustrated for both electrodes.

3 Results and discussion

3.1 Initial characterisation

The results of the initial characterisation of all investigated cells are summarized in the box plots in Fig. 3. The statistical values are given in Table 3, where μ indicates the mean value, med. is the median, σ is the standard deviation and κ is the relative coefficient of variance (rCoV) σ/μ in %.

Table 3 Results of the initial characterisation of 94 cells as described in section 2.3

Parameter	μ	Med.	σ	κ
Capacity	1.16 A h	1.17 A h	0.013 A h	1.15%
$R_{10\%}$[a]	156.7 mΩ	161.5 mΩ	16.3 mΩ	10.39%
$R_{50\%}$[a]	88.3 mΩ	91 mΩ	10.4 mΩ	11.29%
$R_{90\%}$[a]	84 mΩ	86.6 mΩ	10 mΩ	11.87%
R_{ZC}	26 mΩ	25.4 mΩ	1.2 mΩ	4.6%
R_{POL}	70.5 mΩ	73.8 mΩ	13.8 mΩ	19.51%
Mass	36.93 g	36.73 g	0.5032 g	1.36%

[a] $R_{10\%}$, $R_{50\%}$ and $R_{90\%}$ are the DC resistance values at 10%, 50% and 90% SOC, measured after 10 s.

The $\kappa_{R_{\mathrm{DC}}}$ ranges from 10.39% at 10% SOC to 11.87% at 90% SOC. The distribution is shown in Fig. 3(a). Wildfeuer and Lienkamp[38] reviewed 13 studies on cell-to-cell variations of lithium-ion batteries and conducted an additional study on 600 commercial LIBs. They reported that $\kappa_{R_{\mathrm{DC}}}$ spans from 0.68% to 5.8%. It is notable that the studies mentioned by Wildfeuer and Lienkamp[38] all use varying metrics for determination of R_{DC}, such as C-rate or pulse duration. The SIBs in this study show a significantly higher variation in R_{DC} compared to the reported values for LIBs. This may be attributed to the different measurement method for R_{DC} used in this study, as well as generally higher variations in SIB cell production compared to the more mature LIB technology. While Wildfeuer and Lienkamp[38] claim that variances in internal resistance correlate strongly with temperature, we tried to mitigate this. In the initial CU, each cell was cycled 10 times before reaching pulse characterisation, meaning all cells were in the climate chamber for more than 50 h. Additionally, we measured the cell temperature throughout the complete CU as described for the calendar cells in section 2.1. The distribution of the temperature is shown in Fig. 3(b). Since the temperature during pulse testing only varies between 24.9 °C and 25.6 °C due to the well-controlled thermal conditions in the climate chamber during pulse testing, we assume that the great variance in R_{DC} is not caused by temperature differences.

R_{ZC} was only measured at 50% SOC. The distribution is shown in Fig. 3(c) and has a $\kappa_{R_{\mathrm{ZC}}}$ of 4.6%. In the reviewed studies for LIBs, only six studies investigated the impedance of the cells. Wildfeuer and Lienkamp[38] reported a range of $\kappa_{R_{\mathrm{ZC}}}$ from 0.46% to 1.94% and one outlier at 19.47%.[39] The SIBs in this study show a significantly higher variation in R_{ZC} compared to the reported values for LIBs, except for the outlier study.

R_{POL} was only measured at 50% SOC as well. The distribution is shown in Fig. 3(d) and has a $\kappa_{R_{\mathrm{POL}}}$ of 19.51%. Wildfeuer and Lienkamp[38] do not specify this resistance value in their summary. Nonetheless, Schuster *et al.*[40] reported a $\kappa_{R_{\mathrm{POL}}}$ of 4.86% for LIBs in their study. Rumpf *et al.*[41] calculated an R_{POL} value analogous to that of

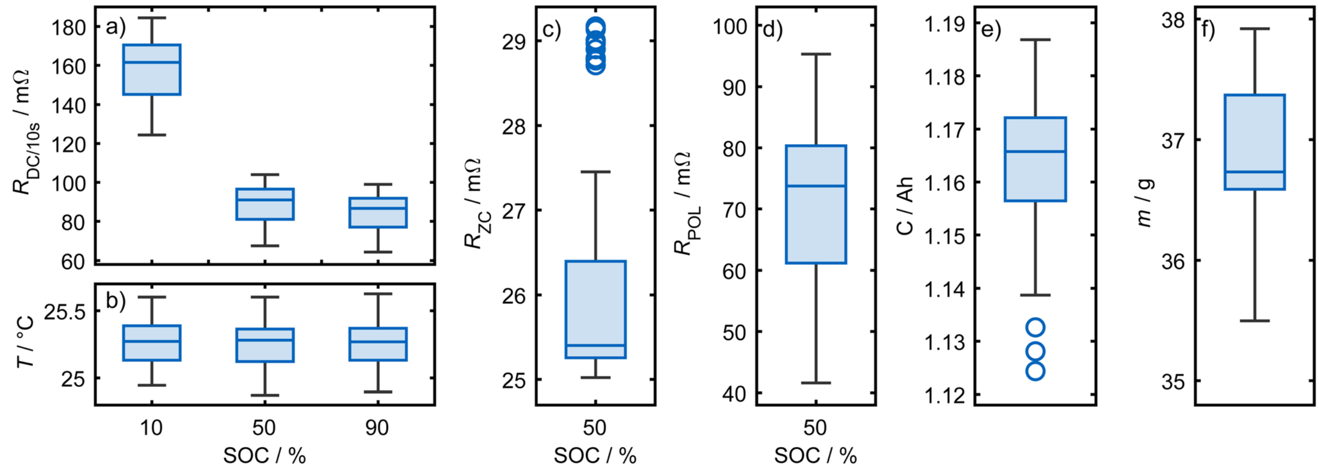

Fig. 3 Distribution of initial measurements: (a) R_{DC} at 10%, 50% and 90% SOC. (b) Cell temperature during pulse measurements. (c) R_{ZC} at 50% SOC. (d) R_{POL} at 50% SOC. (e) Capacity determined during the initial CU. (f) Cell mass measured before cycling. The box spans the interquartile range (Q1–Q3), the line inside the box marks the median, the whiskers extend to the most extreme non-outlier observations within 1.5× the interquartile range of the quartiles, and points beyond the whiskers are plotted as outliers.

Schuster *et al.*[40] and reported a $\kappa_{R_{\mathrm{POL}}}$ of 2.6% and 3.08% for two batches of 1100 LIBs. The variance in R_{POL} for the SIBs in this study is significantly higher than the reported value for LIBs.

The nominal capacity of the 18650-format cell is given as 1.25 A h. The distribution of the capacity of the cells is shown in Fig. 3(e). For the investigated SIB cells in this study, κ_{Cap} is 1.15%. Wildfeuer and Lienkamp[38] reported a variation of κ_{Cap} between 0.16% and 2.36% for all 14 studies. The SIBs in this study lie in the range of the reported values for LIBs. However, no cell reached nominal capacity during initial measurement.

The distribution of the mass of all investigated cells is shown in Fig. 3(f). The mass varies between 35.9 g and 38.1 g with a κ_{mass} of 1.36%.

For LIBs, the influence of initial cell-to-cell variation on degradation has been proven to be non-negligible.[42–44] However the focus in this paper is not to determine the influence of cell-to-cell variation on ageing. We aimed to distribute cell variation homogeneously across all TPs regarding their electrical, electrochemical, and thermal properties.

3.2 Sodium plating and cell selection

The investigated cells in this study show large variances in ageing trajectories even between the same TP. Some cells exhibit a strong decrease in capacity, while others only minor degradation. The problem is exemplified in Fig. 4 for the four cells of TP 8 (20–80% SOC, 1C).

Cell 1 shows a capacity loss of approximately 3.1% after ∼5100 EFCs; cell 4 shows a degradation of approximately 23.4% after ∼3450 EFCs. Some cells show very low coulombic efficiency during CUs. Within the CU procedure, we can analyse the CE during the first two capacity check cycles, $\mathrm{CE_I}$ and $\mathrm{CE_{II}}$. In particular, during the first capacity check cycle, cells 2, 3 and 4 display very low coulombic efficiencies that are below 80%. This indicates that during the charge process, side reactions are occurring. This suspicion is supported by the measured temperature increase during the charging process of both CapCCs. We assume that plating leads to internal short circuits (ISCs), which in turn lead to heating of the cell due to high currents that flow through the small area of the ISC. This in return leads to short-timed high currents through the ISC, which in return might lead to the melting of dendrites due to the high temperature, caused by the current.

Fig. 4 shows a clear correlation between CE and temperature increase during charging. Furthermore, a post-mortem analysis (PMA) of three of the four shown cells confirms sodium plating on the anode of the cells with low CE (cells 2, 3 and 4). In Fig. 8 the anode of cell 1 with high CE exhibits only slight plating on the anode edge while cell 2 reveals increased plating on the edge area and cell 4 shows heavy plating on the whole anode surface.

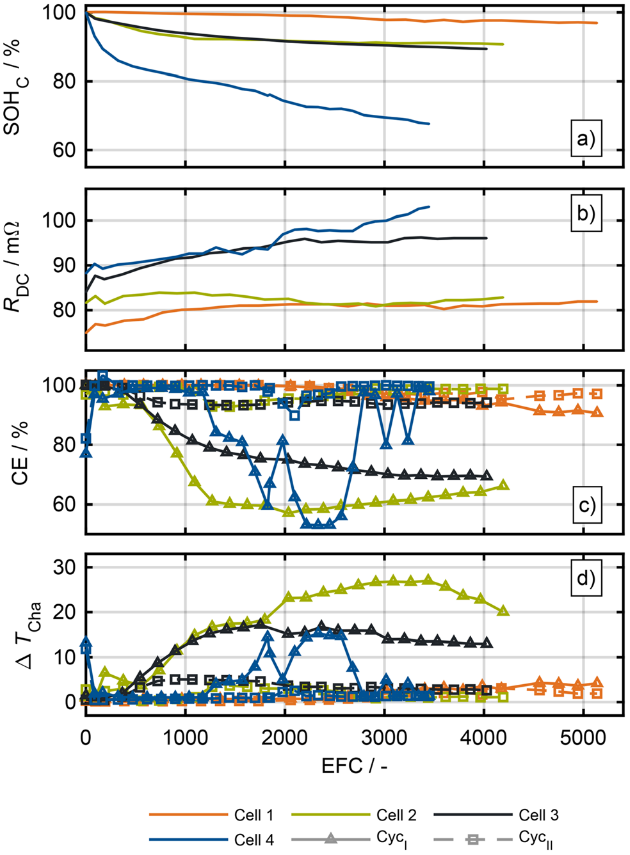

Fig. 4 Check-up results for all cells cycled between 20% and 80% state-of-charge at 1C over EFCs. (a)Variation between cells in terms of capacity state of health. (b) The R_{DC}. (c) The coulombic efficiency during both capacity check cycles of the check-up. (d) The temperature increase during charge of both capacity check cycles of the check-up.

While the CE issue is persistent for cells that show this phenomenon, the degree of low CE fluctuates heavily for some cells, as for example cell 4 in Fig. 4. This cell also shows the highest visible plating in the PMA in Fig. 8. The reason for the fluctuation in CE is unknown and requires further investigation.

The exact mechanism of anode sodiation is still controversially discussed in the literature and depends on the structure of the HC.[5,6,45–48] Authors discuss that the sodiation mechanisms differ between the slope region and plateau region of the anode OCP. Au *et al.*[5] postulate how sodium is first stored in interlayers and on the pore surface of the HC before shifting to pore filling at the plateau region, where sodium is stored in a more metallic state.

Sodium plating on the anode surface is a known degradation mechanism in SIBs. The mechanism of metallic sodium plating on the anode surface is also a point of discussion.[48–50] Hijazi *et al.*[49] conducted a study to investigate the influence of the upper cutoff voltage of an SIB pouch-cell on the plating behaviour at the anode. They also determined the degree of plating *via* the CE during cycling.

They observed a strong increase in plating with increasing upper cutoff voltage. The most pronounced plating in the PMA was found in the cell that was cycled up to 3.95 V across multiple C-rates, while at lower cutoff voltages the extent of plating also increased with increasing C-rate. Liu *et al.*[50] also reviewed the mechanisms of sodium plating on HC anodes in SIBs. They summarized that sodium plating is favoured at high SOC, low temperatures, and high charging rates. They furthermore postulated that plating can be identified by investigating the CE during charge and discharge. Zhou *et al.*[48] reported that the nanopores of HC are not uniformly filled during sodiation, which may in turn lead to sodium plating. They postulated that competing reactions at incompletely filled regions promote sodium plating due to charge transfer, ion conductivity and diffusion inhibitions.

It is evident that the literature does not fully agree on the mechanisms and conditions that lead to plating and cannot substantially provide an exact cause or influence for plating on HC anodes.

Throughout this study, CE issues were observed across all TPs, with some cells plating while others under identical conditions did not. To quantify linear dependencies between initial cell parameters and plating behaviour, the Pearson correlation coefficient r is used, where values close to ± 1 indicate a strong linear relationship and values close to 0 indicate no linear correlation. This raises the question of whether plating can be predicted from the BOT parameters. Fig. 5 shows the average CE per cell plotted against the initial resistance values taken from Table 3. For R_{DC}, a slightly negative correlation is found ($r = -0.675$), suggesting that cells with higher initial resistance face an increased plating risk. Notably, cells with R_{DC} below 75 mΩ appear relatively stable. R_{POL} shows a weaker correlation ($r = -0.587$), while R_{ZC} shows no meaningful correlation ($r = -0.016$). Plating predominantly occurred during the first cycle of the CU. While these results do not allow reliable prediction of plating from initial resistance alone, an elevated R_{DC} can serve as an indicator of increased plating risk.

Since sodium plating significantly influences the ageing behaviour of the cells and leads to non-reproducible results, we selected cells with high CE during the CUs for further analysis of degradation modes. Therefore, for each test point the cell with the highest average CE during CUs is selected for further degradation-mode analysis as described in section 2.5. Only one cell per TP was analysed in the DMA.

The correlation between the ageing rate and the CE is shown in Fig. 11 and 12.

While this selection process neglects cells with significant plating activity to ensure interpretable DMA results, it reduces the number of cells available for statistical evaluation to a single representative cell per test point. Given the observed initial cell-to-cell variability as described in section 3.1, the reported degradation trends should be interpreted with caution, as they may not fully capture the spread of ageing behaviour across the cell population.

It is to be noted that only one cell cycled at 2C could be selected for further analysis, since all other cells of this TP could not be cycled for more than 200 cycles. These cells could not be charged anymore after this point, most likely due to triggering the CID.

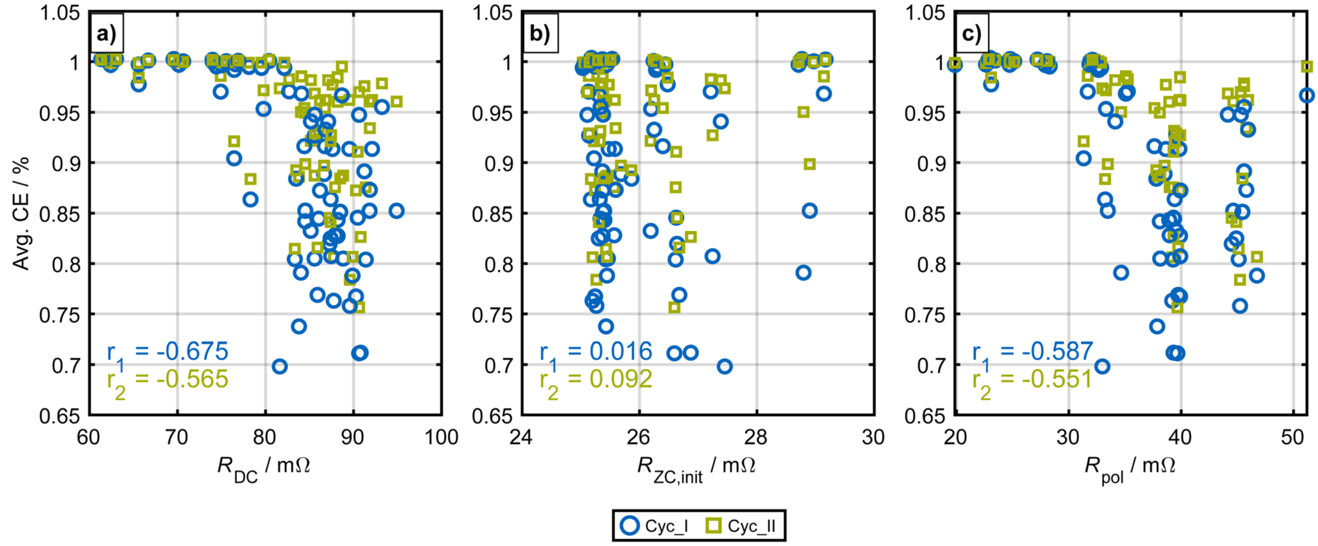

Fig. 5 Correlation between initial resistance values from Table 3 and the mean CE across all CUs of the ageing study. For each cell, the initial resistance (measured prior to cycling) is plotted against the average CE computed over all check-ups. The CE of the first cycle of each CU is shown in blue, the second cycle in green. (a) Correlation with R_{DC} measured at 50% SOC. (b) Correlation with R_{ZC}. (c) Correlation with R_{POL}. The Pearson coefficient is given for each cycle as r_1 and r_2, respectively.

3.3 Ageing behaviour and degradation modes during cycle ageing

The results of the ageing study and DMA are shown in Fig. 6. As described in section 3.2, only one cell per test point is evaluated. In addition, DMA is only performed until an SOH_C of 70% is reached. This is done due to excessive ageing mechanisms and thus increasing RMSEs during fitting. The results are grouped into the three influence categories of cycle ageing investigated in this study: DOD, mean SOC and C-rate. The values for each TP are given in Table 4. Furthermore, the ageing results including the CEs for every cell investigated in this study are given in Fig. 9 and 10.

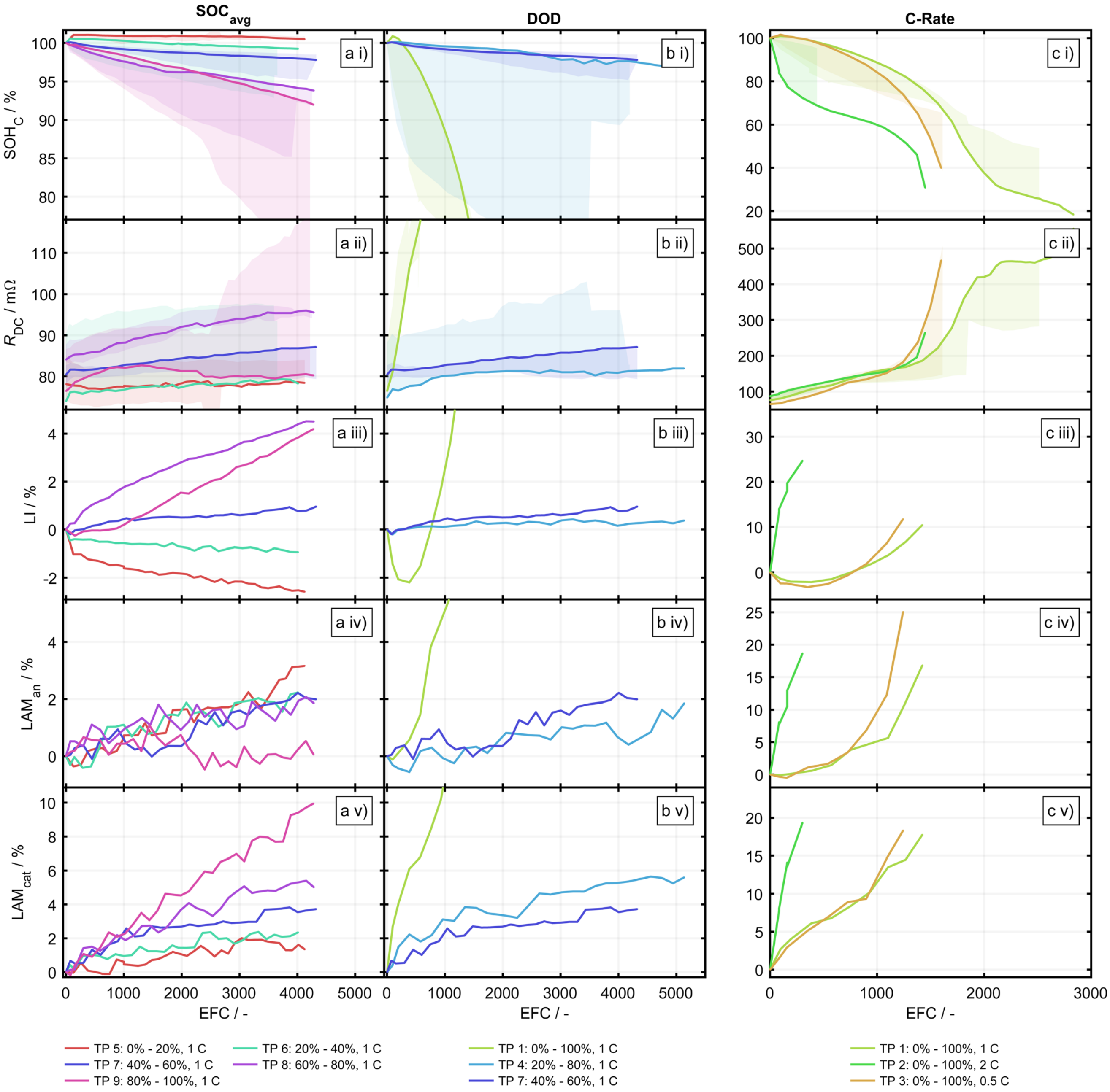

Fig. 6 Cycle ageing results and degradation-mode analysis of selected cells for each test point. Influence of SOC_{avg} at 20% depth of discharge and 1C shown in the left-hand column (a). Influence of depth of discharge around state-of-charge 50% and at 1C shown in the middle column (b). Influence of C-rate at 100% depth of discharge shown in the right-hand column (c). Capacity state of health (i), direct current resistance (ii), loss of charge carrier inventory (iii), loss of active material at the negative electrode (iv), loss of active material at the positive electrode (v). TP 7 is represented in columns (a) and (b). TP 1 is represented in columns (b) and (c). The shaded areas in lines (i) and (ii) span the minimum and maximum values for SOC and R_{DC} during each CU, respectively. The coloured line represents the ageing data of the cell selected for DMA according to the selection process in detailed section 3.2 for each TP.

Table 4 Battery degradation values across test points: total number of EFCs until the EOT, SOH_C, R_{DC} at the BOT and the EOT and the percentage change, and degradation modes

TP	EFCs	SOH_C in %	BOT R_{DC} in mΩ	EOT R_{DC} in mΩ	SOH_R in %	LI in %	LAM_{an} in %	LAM_{cat} in %
1	2835	18.3	76.4	555.2	726.7	10.4	16.8	17.8
2	1449	30.8	87.6	265.0	302.5	24.7	18.7	19.4
3	1600	39.9	65.6	467.3	712.3	11.7	25.1	18.3
4	5136	96.9	74.9	81.9	109.3	0.4	1.9	5.6
5	4127	100.5	78.1	78.4	100.4	−2.6	3.2	1.3
6	4013	99.3	74.0	78.3	105.8	−0.9	2.2	2.3
7	4326	97.8	80.4	87.1	108.3	1.0	2.0	3.7
8	4284	93.8	84.1	95.5	113.6	4.5	1.9	5.0
9	4279	92.0	76.4	80.3	105.1	4.2	0.1	10.0

3.3.1 Influence of mean state-of-charge. The influence of mean SOC during cycle ageing is shown in the left-hand column of Fig. 6a(i)–a(v) for TPs 5–9. All cells show a capacity retention of more than 90% SOH_C after approximately 4200 EFCs. The capacity loss increases proportionally with mean SOC at a constant DOD of 20%. Cells cycled at TP 5 and 6 show an initial increase in capacity before degradation sets in. This might be explained by the anode overhang of the cell.[51–53] Wilhelm *et al.*[53] claim that the equalization of the anode overhang is mainly driven by potential differences between the active anode area and the overhang area during cycling. Streck *et al.*[54] showed in their study, that the anode overhang equalization of SIBs matches those of LIBs. The cells were stored at 50% SOC before the first CU. When cycling in lower SOC ranges, sodium from the overhang area is transferred into the active anode area. This is also in line with the LI results for those cells.[54]

The geometry of the electrode sheets was determined in a previous work. While the area of active material on the anode was measured at 844.29 cm^2, the area of active material on the cathode was measured at 794.6 cm^2. This leads to an overhang area of the anode of 49.64 cm^2.[24] With a cell capacity of 1.2 A h, the theoretical capacity of the overhang—scaled proportionally to its area relative to the total cathode area—amounts to 75 mA h, while storage at 50% SOC would allow a maximum charge of 37.5 mA h in the overhang. The cell cycling between 0% and 20% SOC accumulated approximately 12.3 mA h during cycling. Since the migration of charge into the overhang is a slow process, and not all cyclable sodium is being removed from the overhang at this TP, these values align well with our assumption. Nonetheless, further research into the migration of sodium within the hard carbon overhang is required.

TP8 shows the highest initial capacity loss before the degradation rate decreases after approximately 1800 EFCs. The cell cycled at TP 9 shows a linear degradation of capacity over the whole ageing period and has the highest total degradation in capacity. The initial faster capacity decrease of TP 8 may be caused by the significantly higher R_{DC} at the BOT.

DMA reveals that arguably the most dominant degradation mode is LAM_{cat}. With increasing mean SOC and thus higher voltage levels of the cathode, the LAM_{cat} grows significantly. The LAM_{cat} ranges from 1.35% for TP5 to 9.95% for TP9 at the EOT.

This aligns with the results of Lin *et al.*,[9] who investigated the influence of upper cutoff voltage on the ageing behaviour of SIBs with layered oxide cathodes and HC anodes. With a higher cutoff voltage, the degradation of the cathode accelerates, caused by stronger growth and a more developed cathode electrolyte interphase (CEI) as well as cracking and structural degradation. The CEI thickness ranges from 4.7 nm at 3.8 V to 14.7 nm at 4.0 V and 17 nm at 4.2 V cutoff voltage after 300 cycles. The thicker CEI leads to higher impedance, especially in the charge transfer process. The authors also demonstrated increasing cathode transition metal deposition on the anode with higher cutoff voltages.[9]

Hijazi *et al.*[49] also discuss cathode degradation due to high voltage levels in SIBs. They measured a rise of impedance on the cathode side after cycling to higher cutoff voltages.

Additionally, Habib *et al.*[10] determined that irreversible phase transitions, interlayer strain, and a gradual destabilisation of the layered framework contribute to a loss of electrochemically active material at high voltages.

These results are consistent with our observations.

LAM_{an} shows the opposite trend: higher SOC ranges lead to lower LAM_{an}. This may be explained by the primary sodiation mechanism in the sloping region, where surface adsorption and defect-assisted intercalation dominate the OCP behaviour.[46]

Cycling at low SOC may lead to higher stresses in the anode material during sodiation and desodiation due to the mechanism of the processes in this area. While cycling in low full-cell SOCs, the anode is mainly (de-)sodiated by surface adsorption and defect-assisted intercalation. While plating on the anode surface of HC has been broadly discussed in the literature, mechanical degradation of HC anodes during cycling has rarely been investigated. However, the LAM_{an} is significantly lower than LAM_{cat} for all cells except during TP 5 and ranges from 0.05% to 3.16% at the EOT whereas TPs 6–8 exhibit LAM_{an} between 1.85% and 2.23%.

The LI for all cells lies below the capacity loss and is therefore not the dominant degradation mode causing capacity loss. TPs 5 and 6 gain cyclable sodium throughout ageing according to the DMA results. This is in alignment with the initial increase in capacity observed for these cells and may arguably be explained by anode overhang. The two cells gain 2.58% and 0.93% cyclable sodium at the EOT. Interestingly, TP 8 shows the highest LI with a loss of 4.5% cyclable sodium. This may be explained by the higher R_{DC} at the BOT of this cell. LI may be caused by SEI growth as well as loss of active sodium due to side reactions during cycling. Plating poses another cause for prominent LI and the potential reversibility of Na plating is still under discussion.[49,50]

3.3.2 Influence of depth of discharge. The influence of DOD during cycle ageing is shown in the middle column of Fig. 6b(i)–b(v). For better visualisation, the results are scaled to 20% and 80% DOD, cutting through TP 1. TP 1 is also represented in the right-hand column of Fig. 6. Degradation trajectories for TP 4 and 7 hardly differ from each other. For the following comparison, TP 7 is evaluated at the EOT after approximately 4300 EFCs and TP 4 after approximately 4550 EFCs, which does not reference the EOT of this cell, but is the closest CU point to the EOT of TP 7. TP 4 reaches an SOH_C of 97.2% and TP 7 reaches an SOH_C of approximately 97.8%. The R_{DC} increases from 80.4 mΩ to 87.1 mΩ for TP 7 and from 74.9 mΩ to 81.5 mΩ for TP 4. The R_{DC} for TP 7 increases by 8.3% while the R_{DC} for TP 4 increases by 8.8%. The LI lies between 0.31% and 0.96% at the EOT for both cells. LAM_{an} lies between 1.99% and 1.84%, while LAM_{cat} is slightly higher for TP 4 at 5.6% compared to 3.7% for TP 7. This is in close alignment with the results for mean SOC, which indicate higher voltages lead to greater cathode degradation. The cell cycled with 100% DOD exhibits a significantly higher degradation rate compared to the other DODs and will be discussed further in the following section.

3.3.3 Influence of C-rate. The influence of C-rate during cycle ageing is shown in the right-hand column of Fig. 6c(i)–c(v). All cells at 100% DOD show the highest degradation rates compared to the other influence categories. TP 1 shows the lowest degradation rate, while TP 3 shows the highest degradation rate. It is notable that cells were cycled beyond 70% SOH_C. As described in section 3.2, only one cell could be cycled for more than 200 cycles at a C-rate of 2C. Therefore, only one cell could be subjected to this TP. Additionally, this cell showed strong plating behaviour throughout the ageing study. It shows a very high degradation rate and reaches an SOH_C of 70% after approximately 300 EFCs. Furthermore, the trajectories for all three C-rates differ from each other. While TP 1 and 3 show a similar exponential degradation behaviour, TP 2 shows a polynomial behaviour with accelerated ageing at the beginning, a slower degradation between 300 EFCs and 1050 EFCs before showing signs of an ageing kneepoint, which are also observed with LIBs.[55] In this TP, all degradation modes are significantly higher than in the other influence categories. Cells cycled with C-rate of 1C and 0.5C show an initial gain of cyclable sodium of 3.3% and 2.2% before going into an exponential degradation trajectory. For these TPs, it is unclear whether the initial gain can be explained by anode overhang similar to that described in section 3.3.1. Since we assume that potential differences drive the sodium transfer[53] and the OCP of the anode is in the plateau area at 50% full-cell SOC, the equalization of the anode is triggered more dominantly when cycling in lower SOC ranges. Here, the anode OCP is in the sloping region and thus greater potential differences lead to a stronger driving force for sodium transfer from the overhang area to the active anode area.[52] Therefore, when cycling to 0% SOC, we could expect a stronger effect of anode overhang equalization. LAM_{an} is significantly higher for all cells cycled at 100% DOD compared to the other influence categories. Only when being cycled between 0% and 100% SOC does the LAM_{an} match the LAM_{cat}, whereas cycling within smaller windows results in LAM_{an} being lower than LAM_{cat}. It is to be noted however that cycling at 100% DOD leads to strong degradation for all cells and might thus lead to non-reproducible results.

3.4 Ageing behaviour and degradation modes during calendar ageing

In this section, the ageing behaviour and degradation modes of the cells during calendar ageing are analysed and discussed. The results are shown in Fig. 7. The influence of storage SOC at 25 °C is shown in the left-hand column of Fig. 7 and the influence of storage SOC at 45 °C is shown in the right-hand column. The values for each TP are given in Table 5.

3.4.1 Influence of storage state-of-charge. For cells stored at 25 °C, no clear correlation between storage SOC and degradation rate can be observed. While cells stored at 10%, 30% and 90% SOC show only minor degradation and a correlation between storage SOC and degradation rate, cells stored at 50% and 70% SOC show significantly higher degradation rates. However, this may be caused by cell-to-cell variations as discussed in section 3.1, as those two cells show significantly higher R_{DC} at the BOT compared to the other cells. The initial R_{DC} has been shown repeatedly to influence the ageing behaviour of cells in this work.

Cells stored at 50% and 70% SOC show pronounced LI of 5.2% and 9.23% at EOT compared to the other cells that show LI between −1.32% and 1.68%. It is to be noted that all cells stored at 50% SOC and 70% SOC exhibited the CE problem described in section 3.2 during CU. This indicates that these cells experienced plating during CU, which might lead to increased ageing and LI as well. However, the CE for the 50% SOC cell was worse during all CUs than the CE for the 70% SOC cell, which is not in alignment with the LI results.

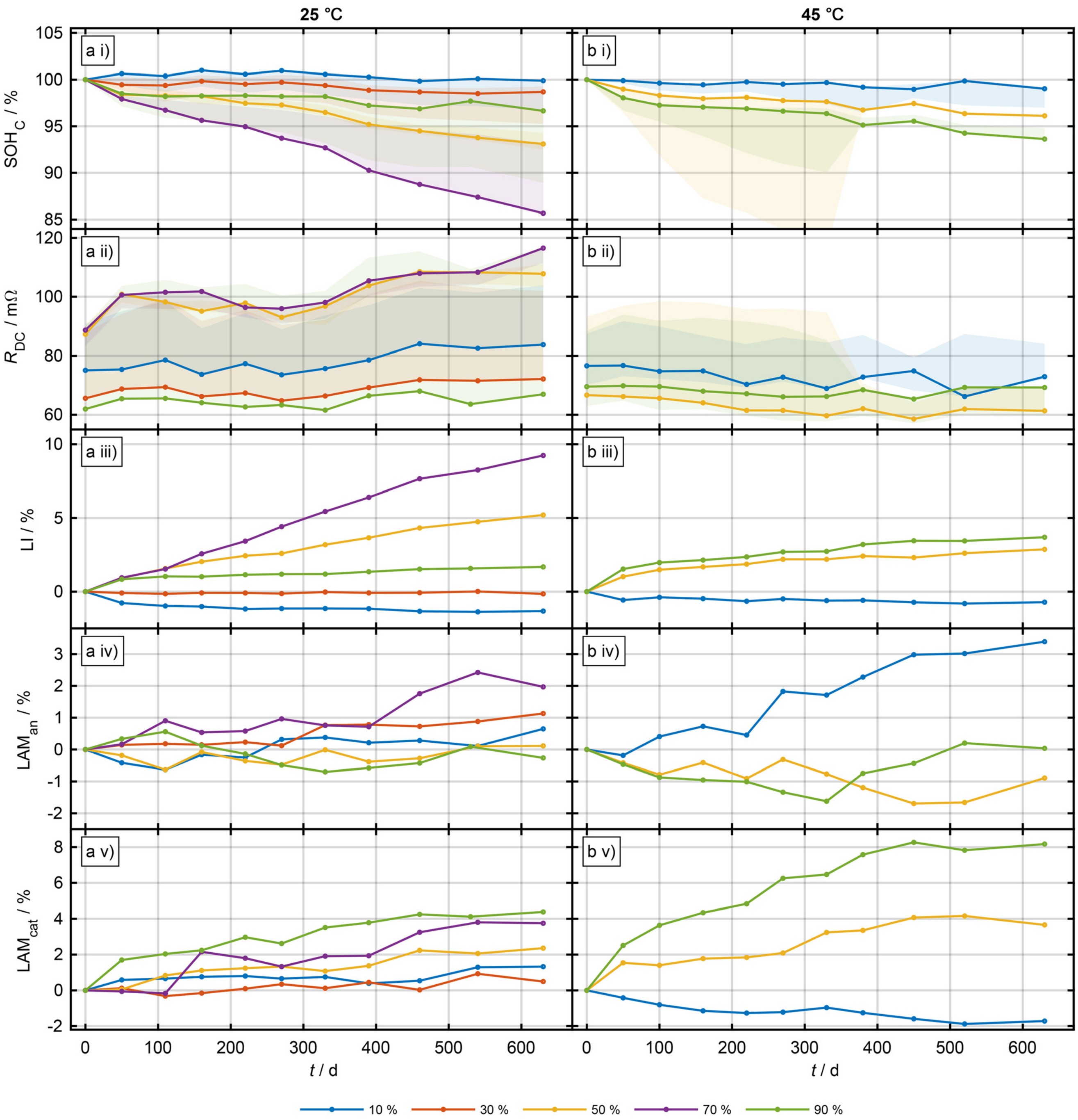

Fig. 7 Calendar ageing results and degradation-mode analysis of selected cells for each test point. Influence of storage state-of-charge at 25 °C is shown in the left-hand column (a). Influence of storage state-of-charge at 45 °C is shown in the right-hand column (b). Capacity state of health (i), direct current resistance (ii), loss of charge carrier inventory (iii), loss of active material at the negative electrode (iv), loss of active material at the positive electrode (v). The shaded areas in lines (i) and (ii) span the minimum and maximum values for SOC and R_{DC} during each CU, respectively. The coloured line represents the ageing data of the cell selected for DMA according to the selection process detailed in section 3.2 for each TP.

For LIBs, SEI growth is known to be the dominant degradation mechanism during calendar ageing.[56] For SIBs, the literature suggests that the SEI is less stable.[57,58] Comparing the TPs at 10%, 30% and 90% SOCs, the LI increases with higher SOC. This could be explained by there being more pronounced SEI growth at higher full-cell voltages, which in turn then dissolves during CU leading to LI. The SEI in SIBs is much more unstable compared to that in LIBs.[58] The cell stored at 10% SOC even shows a slightly negative LI between the initial and first CU, and only changes slightly afterwards. This again can be explained by the anode overhang as detailed in section 3.3.1.

Table 5 Characterisation of battery degradation during calendar ageing after 630 d: state of health, DC resistance, sodium inventory loss, and active material loss at different states of charge

T in °C	SOC in %	SOH_C in %	BOT R_{DC} in mΩ	EOT R_{DC} in mΩ	SOH_R in %	LI in %	LAM_{an} in %	LAM_{cat} in %
25	10	99.9	75.1	83.7	111.5	−1.3	0.6	1.3
	30	98.7	65.6	72.2	110.1	−0.2	1.1	0.5
	50	93.1	87.3	107.8	123.5	5.2	0.1	2.4
	70	85.7	88.7	116.5	131.3	9.2	2.0	3.8
	90	96.7	61.3	67.0	109.2	1.7	−0.3	4.4
45	10	99.0	76.6	72.9	95.2	−0.7	3.4	−1.7
	50	96.1	66.7	61.3	91.9	2.9	−0.9	3.7
	90	93.6	69.5	69.3	99.7	3.7	0.0	8.2

The LAM_{an} is low for all cells ranging from −0.26% to 1.97% at the EOT. Interestingly, the LAM_{cat} shows a slightly more prominent correlation with storage SOC, ranging from 0.49% at 30% SOC being the lowest, to 4.38% at 90% SOC at the EOT. Here, a correlation between higher cathode voltage and higher LAM_{cat} can be observed as discussed in section 3.3.1. Faster ageing of cells at 50% and 70% SOC therefore seems to be triggered by LI.

For cells stored at 45 °C, a clear correlation between storage SOC and degradation rate can be observed. The cell stored at 10% SOC exhibits the lowest degradation rate while the cell stored at 90% SOC exhibits the highest degradation rate. While R_{DC} does not change significantly, LI increases with higher storage SOC. Again, the cell stored at 10% SOC shows a slightly negative LI before neither gaining nor losing significant amounts of LI throughout ageing. LAM_{an} and LAM_{cat} correlate with the storage SOC. Higher storage SOC leads to higher LAM_{cat}, while the LAM_{an} is highest for the cell stored at 10% SOC. Cells stored at higher SOC show slightly negative LAM_{an}, while the LAM_{cat} is significantly higher for storage at 90% SOC. The LAM_{cat} is in alignment with the results discussed in section 3.3.1, which states that higher SOCs lead to higher degradation of the cathode material.

3.4.2 Influence of storage temperature. To investigate the influence of storage temperature during calendar ageing, cells were stored at 25 °C and 45 °C at 10%, 50% and 90% SOC. Since the cells stored at 25 °C and 50% SOC all showed low CE behaviour, which indicates plating and thus excessive degradation, this SOC will be excluded from this comparison. Cells stored at 45 °C show slightly higher degradation rates compared to the cells stored at 25 °C. While the cell stored at 10% SOC and 25 °C shows a capacity retention of 99.9% at the EOT, the cell stored at 10% SOC and 45 °C shows a capacity retention of 99.0% at the EOT. The cell stored at 90% SOC and 25 °C shows a capacity retention of 96.9% at the EOT, while the cell stored at 90% SOC and 45 °C shows a capacity retention of 93.6% at the EOT. Since only two storage temperatures were investigated, no general conclusions regarding the temperature dependence of degradation kinetics can be drawn. However, the results indicate that higher storage temperatures lead to higher degradation rates during calendar ageing of SIBs. In particular, the correlation of loss of active material and storage SOC is more pronounced at 45 °C compared to that at 25 °C. For a temperature of 45 °C, the cell stored at 10% SOC reveals the highest LAM_{an} of all investigated calendar cells, whereas the cell stored at 90% SOC exhibits the highest LAM_{cat} of all investigated calendar cells.

LI is also slightly higher when the cells are stored at higher temperature. This might be attributed to higher instability of the SEI at higher temperatures.

4 Conclusion

In this work, we present a comprehensive ageing study on commercial sodium-ion batteries featuring layered-oxide cathodes and a hard-carbon anode. We stored cells for more than 600 days for calendar ageing and cycled cells for up to 5000 equivalent full cycles during cycle ageing tests. Initial characterisation revealed pronounced cell-to-cell variability in both capacity and impedance, exceeding what is typically observed for lithium-ion batteries.

Calendar and cycle ageing were investigated across different state-of-charge windows, depth of discharges, C-rates, and temperatures. Even under identical test protocols, the cells exhibited strongly divergent ageing trajectories. We identified metallic sodium plating on the anode as a relevant parasitic side reaction during charging. To analyse the intrinsic degradation pathways, the main degradation modes were evaluated by degradation-mode analysis for cells that showed no or only minimal plating during check-ups.

Loss of active material at the cathode is the dominant degradation mode at high state-of-charges, consistent with the literature on layered-oxide sodium-ion batteries. In contrast, loss of active material at the anode became more pronounced at lower state-of-charges. The mechanistic origin of this increased anode degradation under low state-of-charge cycling and storage requires further investigation. Notably, loss of charge carrier inventory is not the dominant degradation mode in these sodium-ion batteries, in contrast to many lithium-ion battery studies.

Overall, this work provides experimentally grounded insights into the ageing behaviour of commercial sodium-ion batteries with layered-oxide cathodes and hard-carbon anodes. The findings support the development of operating strategies —particularly regarding state-of-charge management and charging conditions—to mitigate degradation and extend cell lifetime.

Furthermore, future studies should investigate the temperature dependence of degradation across at least three temperature levels to enable a more robust characterisation of thermal activation behaviour in sodium-ion batteries.

Author contributions

Julius Bahrke: conceptualisation, software, data curation, visualization, writing – original draft, writing – review & editing. Mathias Rehm: conceptualisation, methodology, data curation, writing – original draft, writing – review & editing. Johannes Natterer: methodology, data curation, writing – review & editing. Caroline Wendlandt: data curation, writing – review & editing. Andreas Jossen: supervision, writing – review & editing.

Conflicts of interest

The authors declare that they have no known competing financial interests or personal relationships that could have appeared to influence the work reported in this paper.

Data availability

The data used in this article is available at https://doi.org/10.14459/2026mp1840745.

The data includes (i) the initial check-ups described in the paper, (ii) the check-ups throughout the ageing study described in the paper, (iii) the results of the degradation-mode analysis performed during the check-ups of (ii).

Appendices

Appendix: Post-mortem analysis

The post-mortem analysis of anodes from cells of TP 8 after cycle ageing is shown in Fig. 8.

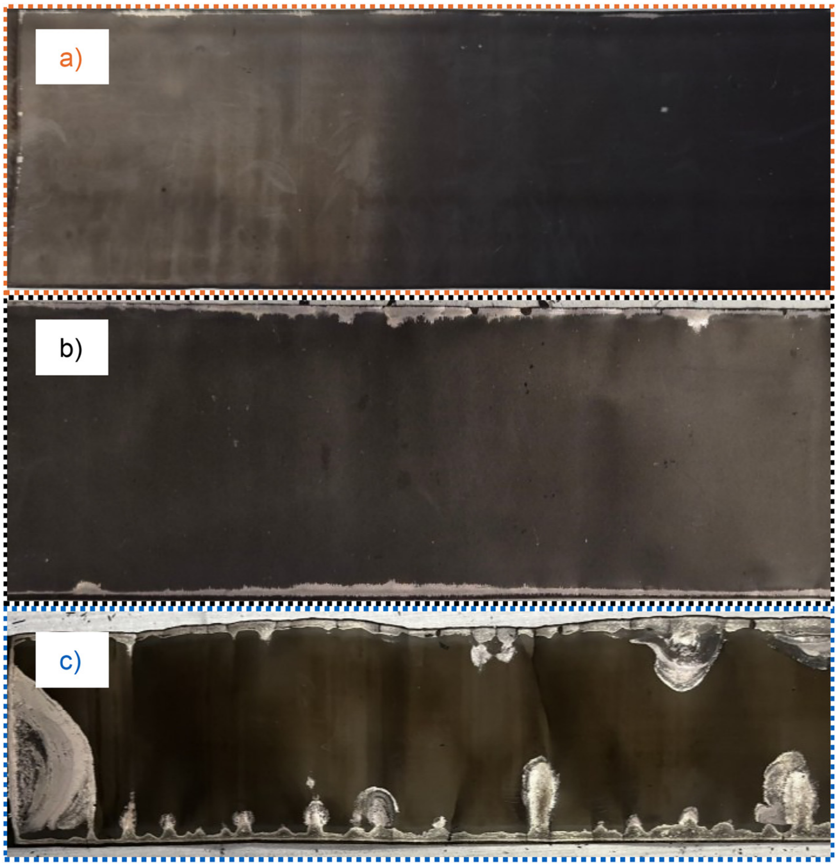

Fig. 8 Post-mortem analysis of anodes from cells of TP 8 after cycle ageing. (a) Cell 1 with high CE during CUs shows small amounts of sodium plating. (b) Cell 2 with low CE during CUs showing increased plating at the anode edge. (c) Cell 4 with low CE during CUs showing heavy sodium plating on the anode surface.

Appendix: All ageing data

The ageing results including the CEs for every cell investigated in this study are given in Fig. 9 and 10.

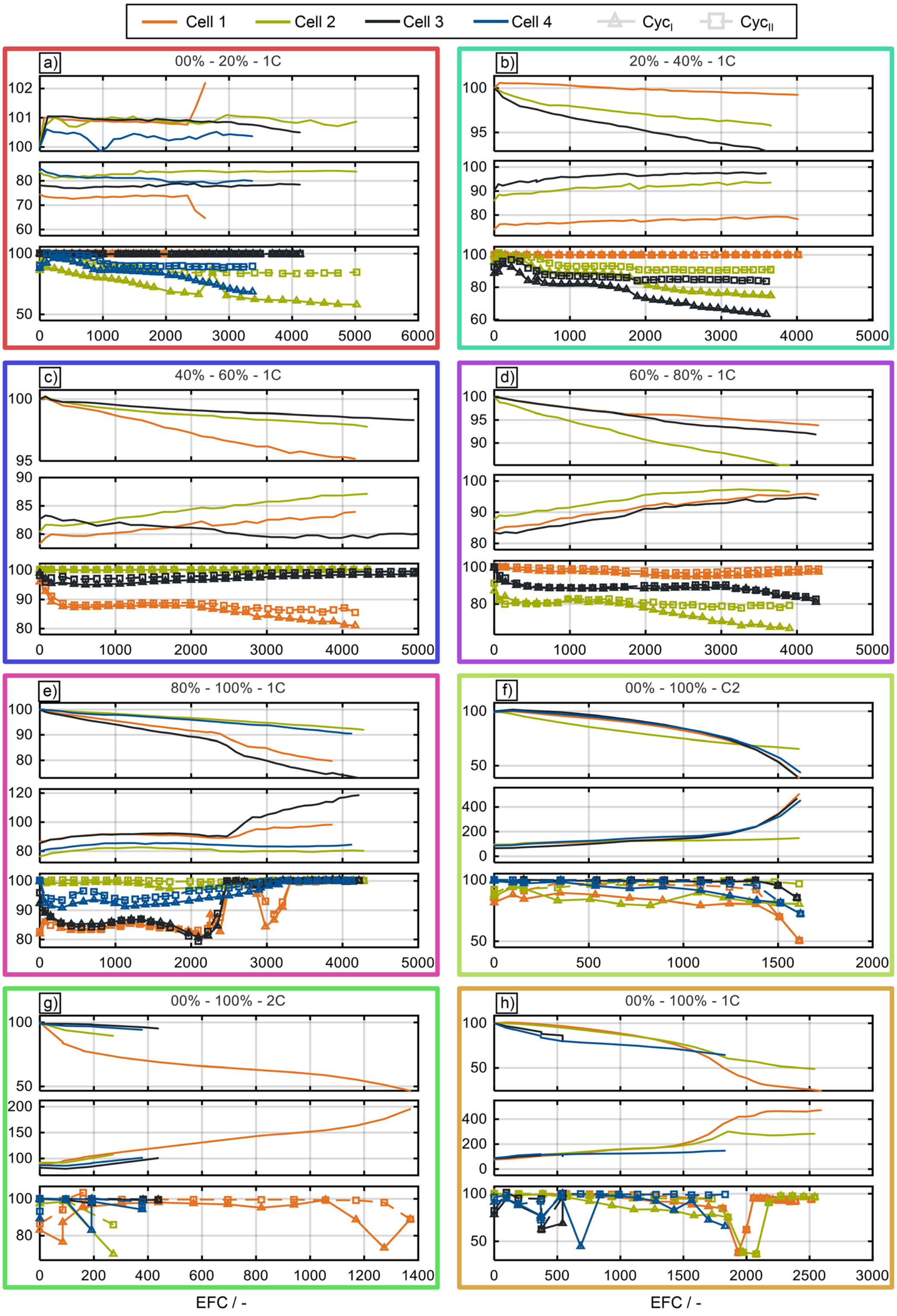

Fig. 9 Results for all cells during cycle ageing. The frame colour corresponds to the colour of each TP in Fig. 6. Each subplot is structured as Fig. 4.

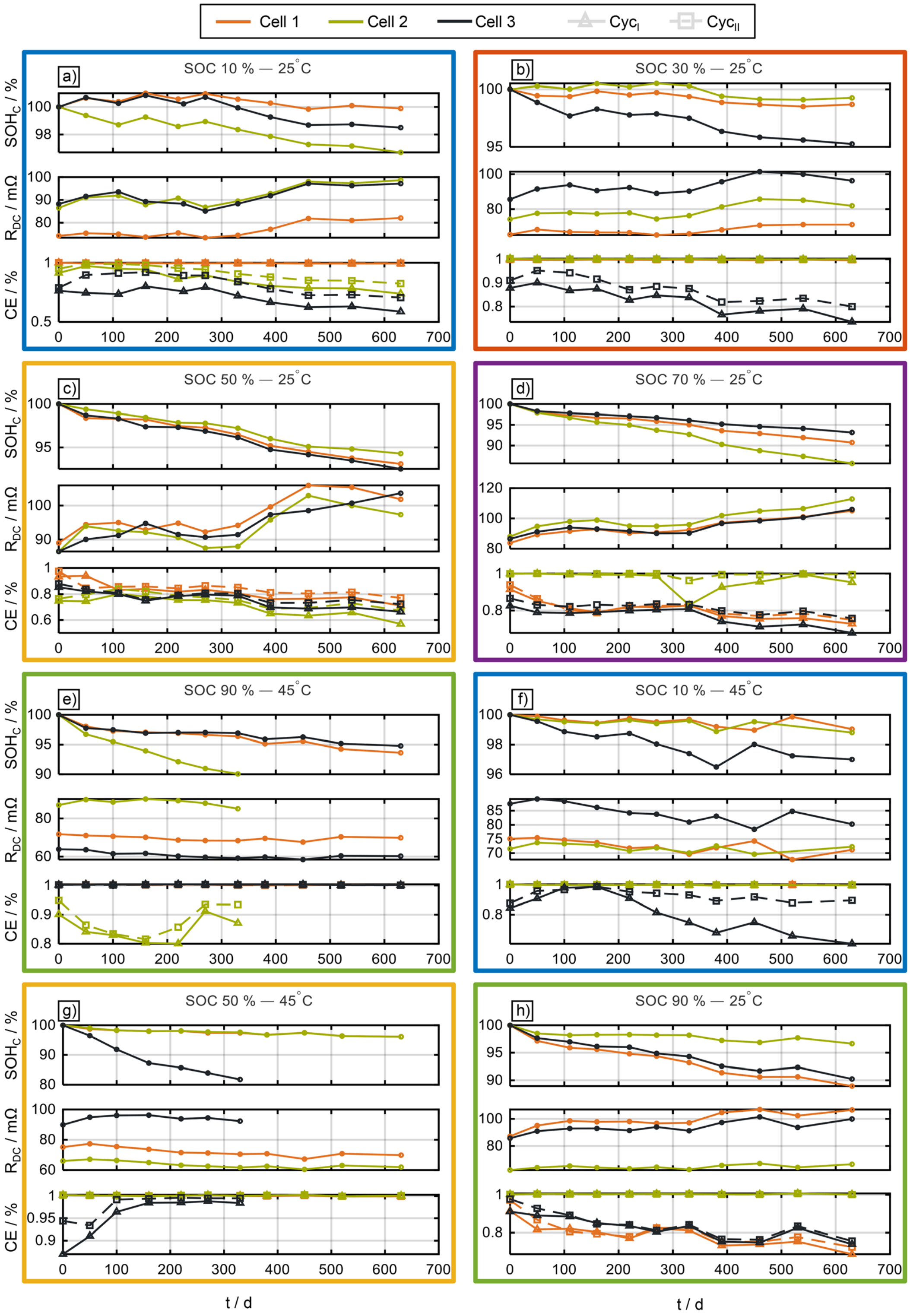

Fig. 10 Results for all cells during calendar ageing. The frame colour corresponds to the colour of each TP in Fig. 7. Each subplot is structured as Fig. 4.

Appendix: Influence of CE on ageing rate

The correlation between the ageing rate and the CE is shown in Fig. 11 and 12.

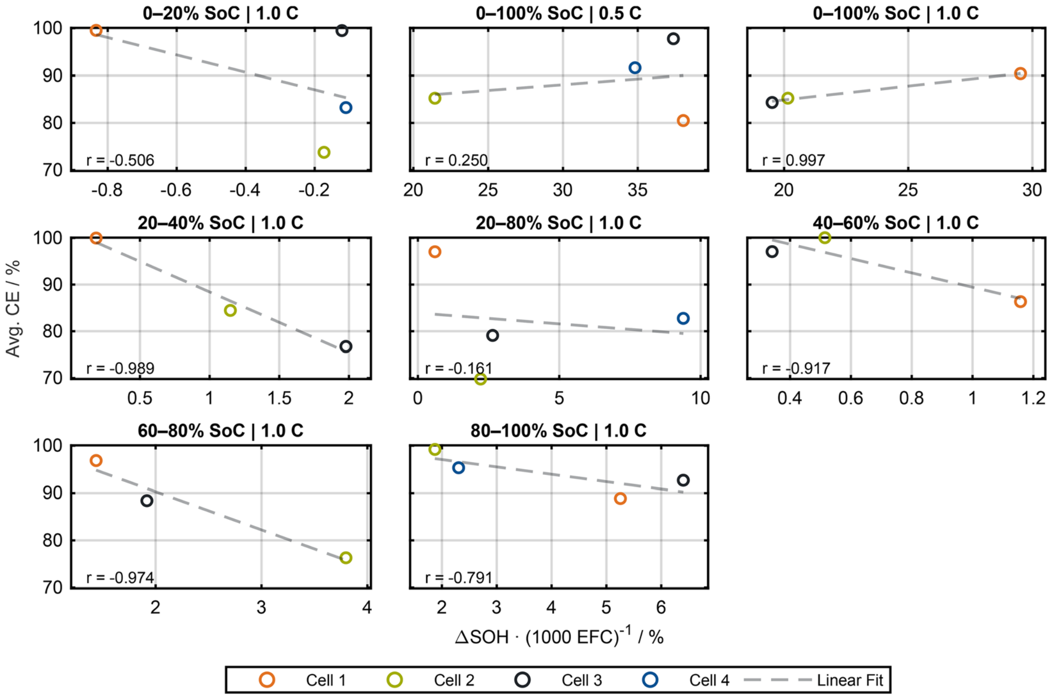

Fig. 11 Correlation between average CE and SOH_C degradation rate during cycle ageing. The degradation rate is defined as the linear slope between the BOT and the EOT SOH_C values, normalised to 1000 EFCs. Each TP is shown individually, with marker colours corresponding to those in Fig. 9. The dashed line represents the linear fit, with the Pearson coefficient *r* given in each panel.

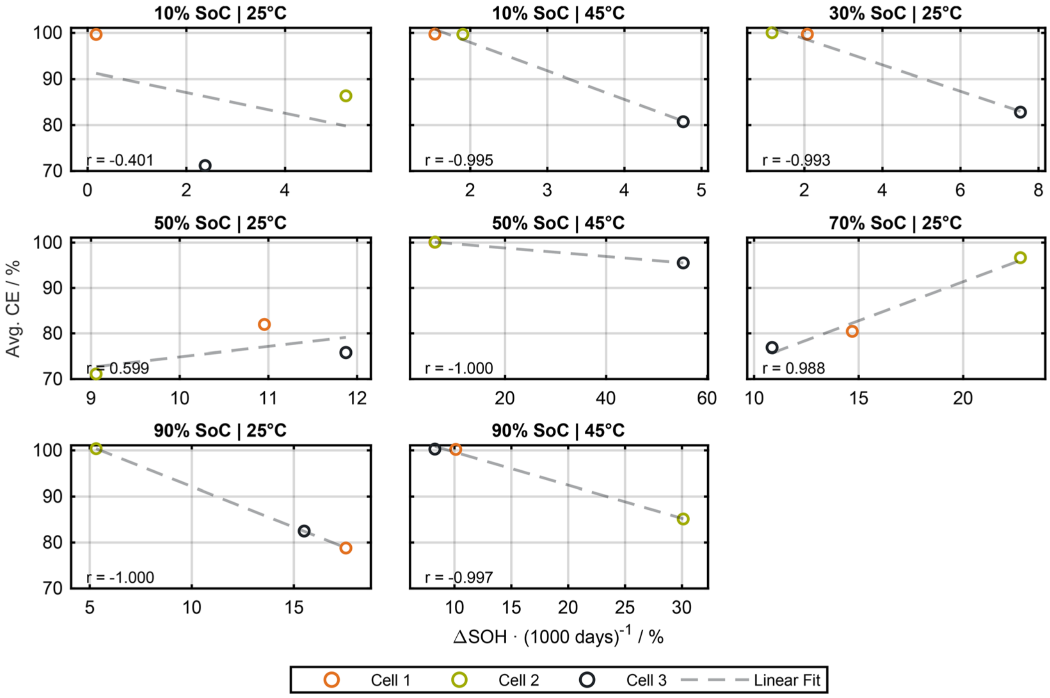

Fig. 12 Correlation between average CE and SOH_C degradation rate during calendar ageing. The degradation rate is defined as the linear slope between the BOT and the EOT SOH_C values, normalised to 1000 days. Each TP is shown individually, with marker colours corresponding to those in Fig. 9. The dashed line represents the linear fit, with the Pearson coefficient *r* given in each panel.

Acknowledgements

This research was financially supported by the Federal Ministry for Economic Affairs and Energy under the project 03EI4041B BoLeRo and by the Technical University of Munich. The responsibility for this publication rests with the authors. The fruitful discussions with Luis Kitsu Iglesias, Lara Link, Axel Durdel, Veronika Vachenauer and Alexander Karger are gratefully acknowledged. We would like to thank students Leon Milutinovic and Igor Brakus for their work in this project.

During the preparation of this work, the authors used Grammarly and ChatGPT for individual sections to improve language and readability. After using these tools, the authors reviewed and edited the content as needed and take full responsibility for the content of the publication.

References

1 M. Wentker, M. Greenwood, M. C. Asaba and J. Leker, *J. Energy Storage*, 2019, **26**, 101022.
2 P. K. Nayak, L. Yang, W. Brehm and P. Adelhelm, *Angew. Chem., Int. Ed.*, 2018, **57**, 102–120.
3 N. Tapia-Ruiz, A. R. Armstrong, H. Alptekin, M. A. Amores, H. Au, J. Barker, R. Boston, W. R. Brant, J. M. Brittain, Y. Chen, M. Chhowalla, Y.-S. Choi, S. I. R. Costa, M. Crespo Ribadeneyra, S. A. Cussen, E. J. Cussen, W. I. F. David, A. V. Desai, S. A. M. Dickson, E. I. Eweka, J. D. Forero-Saboya, C. P. Grey, J. M. Griffin, P. Gross, X. Hua, J. T. S. Irvine, P. Johansson, M. O. Jones, M. Karlsmo, E. Kendrick, E. Kim, O. V. Kolosov, Z. Li, S. F. L. Mertens, R. Mogensen, L. Monconduit, R. E. Morris, A. J. Naylor, S. Nikman, C. A. O'Keefe, D. M. C. Ould, R. G. Palgrave, P. Poizot, A. Ponrouch, S. Renault, E. M. Reynolds, A. Rudola, R. Sayers, D. O. Scanlon, S. Sen, V. R. Seymour, B. Silván, M. T. Sougrati, L. Stievano, G. S. Stone, C. I. Thomas, M.-M. Titirici, J. Tong, T. J. Wood, D. S. Wright and R. Younesi, *J. Phys.: Energy*, 2021, **3**, 031503.
4 S. Roberts and E. Kendrick, *Nanotechnol., Sci. Appl.*, 2018, **11**, 23–33.
5 H. Au, H. Alptekin, A. C. S. Jensen, E. Olsson, C. A. O'Keefe, T. Smith, M. Crespo-Ribadeneyra, T. F. Headen, C. P. Grey, Q. Cai, A. J. Drew and M.-M. Titirici, *Energy Environ. Sci.*, 2020, **13**, 3469–3479.
6 L. Kitsu Iglesias, E. N. Antonio, T. D. Martinez, L. Zhang, Z. Zhuo, S. J. Weigand, J. Guo and M. F. Toney, *Adv. Energy Mater.*, 2023, **13**, 2302171.
7 L. Habib, G. Suo, N. Habib, M. Aqdas, C. Lin, J. Li and S. Javed, *J. Energy Storage*, 2025, **139**, 118821.
8 J. Li, G. Suo, C. Lin, J. Li, X. Luo, G. Yang, L. Habib, Z. K. Kalkozova and K. Naseem, *Chem. Eng. J.*, 2026, **529**, 173031.
9 S. Lin, W. Li, H. Yang, M. Chen, H. Xie, Y. Qin, J. Zeng, P. Zhang and J. Zhao, *EES Batteries*, 2025, **1**, 935–946.
10 L. Habib, G. Suo, J. Li, C. Lin, X. Luo, G. Yang, Z. K. Kalkozova and K. Naseem, *Energy Storage Mater.*, 2026, **84**, 104863.
11 M. Naumann, M. Schimpe, P. Keil, H. C. Hesse and A. Jossen, *J. Energy Storage*, 2018, **17**, 153–169.
12 M. Naumann, F. B. Spingler and A. Jossen.
13 L. Wildfeuer, A. Karger, D. Aygül, N. Wassiliadis, A. Jossen and M. Lienkamp, *J. Power Sources*, 2023, **560**, 232498.
14 N. Kirkaldy, M. A. Samieian, G. J. Offer, M. Marinescu and Y. Patel, *J. Power Sources*, 2024, **603**, 234185.
15 V. Vachenauer, A. Karger, M. Naumann, A. Durdel and A. Jossen, *J. Power Sources*, 2025, **654**, 237779.
16 C. R. Birkl, M. R. Roberts, E. McTurk, P. G. Bruce and D. A. Howey, *J. Power Sources*, 2017, **341**, 373–386.
17 I. Bloom, A. N. Jansen, D. P. Abraham, J. Knuth, S. A. Jones, V. S. Battaglia and G. L. Henriksen, *J. Power Sources*, 2005, **139**, 295–303.
18 J. Schmitt, M. Schindler, A. Oberbauer and A. Jossen, *J. Power Sources*, 2022, **532**, 231296.
19 M. Dubarry, C. Truchot and B. Y. Liaw, *J. Power Sources*, 2012, **219**, 204–216.
20 M. Rehm, J. Bahrke, J. Natterer, L. Milutinovic, F. Roehrer and A. Jossen, *EES Batteries*, 2026, **2**, 665–682.
21 H. Laufen, S. Klick, H. Ditler, K. L. Quade, A. Mikitisin, A. Blömeke, M. Schütte, D. Wasylowski, M. Sonnet, L. Henrich, A. Schwedt, G. Stahl, F. Ringbeck, J. Mayer and D. U. Sauer, *Cell Rep. Phys. Sci.*, 2024, **5**, 101945.
22 S. Klick, H. Laufen, M. Schütte, B. Qian, K. L. Quade, C. Rahe, M. Dubarry and D. U. Sauer, *Batteries Supercaps*, 2025, **8**, e202400546.
23 M. Dubarry and D. Beck, *J. Electrochem. Soc.*, 2024, **171**, 080541.
24 M. Rehm, M. Fischer, M. R. Gomez, M. Schütte, D. U. Sauer and A. Jossen, *J. Power Sources*, 2025, **633**, 236290.
25 M. R. Gomez, S. Ludwig, P. Jocher, A. Frank, Y. Fedoryshyna and A. Jossen, *J. Energy Storage*, 2025, **123**, 116640.
26 P. Jocher, F. Roehrer, M. Rehm, T. Idrizi, A. Himmelreich and A. Jossen, *J. Energy Storage*, 2024, **98**, 112931.
27 Y. Fedoryshyna, S. Schaeffler, J. Soellner, E. I. Gillich and A. Jossen, *J. Power Sources*, 2024, **615**, 235064.
28 M. Schütte, H. Laufen, D. Luder, H. Ditler, J. Kern, S. Klick, M. Junker, G. Stahl, F. Frie and D. U. Sauer, *J. Energy Storage*, 2025, **107**, 114931.
29 F. Roehrer, P. Jocher, M. Rehm, A. Graule and A. Jossen, *J. Power Sources*, 2025, **640**, 236573.
30 F. A. Dorau, A. Sommer, J. Koloch, R. Röß-Ohlenroth, M. Schreiber, M. Neuner, K. Abo Gamra, Y. Lin, J. Schöberl, P. Bilfinger, S. Grabmann, B. Stumper, L. Katzenmeier, M. Lienkamp and R. Daub, *J. Electrochem. Soc.*, 2024, **171**, 090521.
31 E. Irujo, A. Berrueta, P. Sanchis and A. Ursúa, 2024 International Conference on Renewable Energies and Smart Technologies (REST), 2024, pp. 1–5.
32 C. Jiang, Y. Wang, Z. Sun and Z. Chen, *J. Energy Storage*, 2025, **105**, 114552.

33 M. Baumann, L. Wildfeuer, S. Rohr and M. Lienkamp, *J. Energy Storage*, 2018, **18**, 295–307.

34 M. Fischer, M. J. Brand, A. Karger, M. R. Gomez, M. Rehm, J. Natterer and A. Jossen, *J. Power Sources*, 2025, **656**, 237921.

35 W. Waag, S. Käbitz and D. U. Sauer, *Appl. Energy*, 2013, **102**, 885–897.

36 P. Iurilli, C. Brivio and V. Wood, *J. Power Sources*, 2021, **505**, 229860.

37 J. Schmitt, M. Rehm, A. Karger and A. Jossen, *J. Energy Storage*, 2023, **59**, 106517.

38 L. Wildfeuer and M. Lienkamp, *eTransportation*, 2021, **9**, 100129.

39 Y. Zheng, X. Han, L. Lu, J. Li and M. Ouyang, *J. Power Sources*, 2013, **223**, 136–146.

40 S. F. Schuster, M. J. Brand, P. Berg, M. Gleissenberger and A. Jossen, *J. Power Sources*, 2015, **297**, 242–251.

41 K. Rumpf, M. Naumann and A. Jossen, *J. Energy Storage*, 2017, **14**, 224–243.

42 A. Devie, G. Baure and M. Dubarry, *Energies*, 2018, **11**, 1031.

43 T. Baumhöfer, M. Brühl, S. Rothgang and D. U. Sauer, *J. Power Sources*, 2014, **247**, 332–338.

44 O. Makan, M. Gossen and K.-P. Birke, *Energy Rep.*, 2024, **11**, 2003–2010.

45 Q. Xia, C.-L. Ko, E. R. Cooper, Q. Gu, R. Knibbe and J. R. Harmer, *Adv. Funct. Mater.*, 2025, **35**, 2421976.

46 L. Kitsu Iglesias, S. D. Marks, N. Rampal, E. N. Antonio, R. Ferreira de Menezes, L. Zhang, D. Olds, S. E. Weitzner, K. G. Sprenger, L. F. Wan and M. F. Toney, *Small*, 2025, **21**, 2505561.

47 D. Alvira, D. Antorán and J. J. Manyà, *Chem. Eng. J.*, 2022, **447**, 137468.

48 H. Zhou, Y. Song, B. Zhang, H. Sun, I. A. Khurshid, Y. Kong, L. Chen, L. Cui, D. Zhang, W. Wang, L. Yang and X. Du, *Energy Storage Mater.*, 2024, **71**, 103645.

49 H. Hijazi, Z. Ye, L. Zhang, J. Deshmukh, M. B. Johnson, J. R. Dahn and M. Metzger, *J. Electrochem. Soc.*, 2023, **170**, 070512.

50 F. Liu, Z. Chen, Y. Li, L. Fu, J. Ju, J. Ma and Y. Sun, *Nanoscale Horizons*, 2025, **11**, 62–84.

51 M. Lewerenz, G. Fuchs, L. Becker and D. U. Sauer, *J. Energy Storage*, 2018, **18**, 149–159.

52 T. Roth, L. Streck, N. Mujanovic, M. Winter, P. Niehoff and A. Jossen, *J. Electrochem. Soc.*, 2023, **170**, 080524.

53 J. Wilhelm, S. Seidlmayer, P. Keil, J. Schuster, A. Kriele, R. Gilles and A. Jossen, *J. Power Sources*, 2017, **365**, 327–338.

54 L. Streck, T. Roth, H. Bosch, C. Kirst, M. Rehm, P. Keil and A. Jossen, *J. Electrochem. Soc.*, 2024, **171**, 080531.

55 P. M. Attia, A. Bills, F. Brosa Planella, P. Dechent, G. dos Reis, M. Dubarry, P. Gasper, R. Gilchrist, S. Greenbank, D. Howey, O. Liu, E. Khoo, Y. Preger, A. Soni, S. Sripad, A. G. Stefanopoulou and V. Sulzer, *J. Electrochem. Soc.*, 2022, **169**, 060517.

56 A. Karger, S. E. J. O'Kane, M. Rogge, C. Kirst, J. P. Singer, M. Marinescu, G. J. Offer and A. Jossen, *J. Electrochem. Soc.*, 2024, **171**, 090512.

57 R. Mogensen, D. Brandell and R. Younesi, *ACS Energy Lett.*, 2016, **1**, 1173–1178.

58 C. R. Lee, J. Byun, M. Kim, M. A. Lee, C. Hwang, J. H. Song, H. Kim, Y. Kim, J.-S. Yu and H.-s. Kim, *ACS Mater. Lett.*, 2024, **6**, 772–779.